

Dynamic Modeling and Simulation of a Yaw-Angle Quadruped Maneuvering With a Planar Robotic Tail

William Rone

Robotics and Mechatronics Laboratory,
Department of Mechanical Engineering,
Virginia Tech,
Randolph Hall, Room No. 8,
460 Old Turner Street,
Blacksburg, VA 24061
e-mail: wsrone@vt.edu

Pinhas Ben-Tzvi

Mem. ASME
Robotics and Mechatronics Laboratory,
Department of Mechanical Engineering,
Virginia Tech,
Goodwin Hall, Room No. 456
635 Prices Fork Road,
Blacksburg, VA 24061
e-mail: bentzvi@vt.edu

This paper analyzes the impact a planar robotic tail can have on the yaw-angle maneuvering of a quadruped robot. Tail structures ranging from a one degree-of-freedom (1DOF) pendulum to a 6DOF serpentine robot are simulated, along with a quadruped model that accounts for ground contact friction. Tail trajectory generation using split-cycle frequency modulation is used to improve net quadruped rotation due to the tail's motion. Numerical results from the tail and quadruped models analyze the impact of trajectory factors and tail structure on the net quadruped rotation. Results emphasize the importance of both tangential and centripetal tail loading for tail trajectory planning and show the benefit of a multi-DOF tail. [DOI: 10.1115/1.4033103]

1 Introduction and Background

In nature, animals' tails aid in both maneuvering and stabilization. In terms of maneuvering, tails are used by cheetahs to turn while running [1], geckos to reorient while jumping [2], and alligators to assist in rolling while attacking prey [3]. In terms of stabilization, tails are used by house cats to maintain balance [4], kangaroos as a fifth leg while running [5], and monkeys to aid in climbing [6]. Based on these observations, robotics researchers have attempted to imitate these structures onboard robotic systems.

The primary focus of robotics research into tail-like structures has been implementing single-DOF pendulums for a specific function: pitch control in legged [2,7], wheeled [8] and jumping [9–11] robots, actuating walking [12] and climbing [13], yaw-angle turning [14,15], rapid acceleration/deceleration [16], and stabilizing disturbances [17,18]. Multi-DOF tail research has been more limited [19].

Likewise, the field of hyper-redundant robotics, including both serpentine [20,21] and continuum [22,23] robots, exhibits structures that are inherently similar to biological tails with

deformation along the structure's length and the ability to exhibit multiple mode shapes.

This paper analyzes and compares the effect of inertial loading generated by planar tail structures ranging from 1DOF to 6DOF on the resulting net quadruped yaw rotation. In addition, it also studies the impact of various trajectory parameters on the quadruped's net rotation.

2 Mathematical Model

This section presents the mathematical model for the six tail structures and quadruped, including system kinematics and dynamics.

2.1 Quadruped and Tail Kinematics. Six tail structures, illustrated in Fig. 1(a), are considered to study the impact of tail structure (i.e., pendulum versus serpentine) on performance. Figure 1(b) illustrates the 6DOF tail mounted on the quadruped model considered in this analysis. Initially, a flywheel structure was also considered, but preliminary simulations showed a significant reduction in performance compared to pendulum structures. This is because the flywheel's applied loading is purely a moment—no inertial forces are generated. As a result, the applied loading with respect to the system COM is constant regardless of where the flywheel is placed; the flywheel's positioning only impacts the body-fixed position of the net system COM.

Figure 2 illustrates the model variables and reference frames for the kinematic analysis, with a two-link tail shown. Model variables are the three planar quadruped DOF (translations x and y , rotation φ) and n tail joint angles θ_i , $i = \{1, \dots, n\}$ between link $i - 1$ and i (the quadruped is considered link 0). Relative to the ground frame xyz , the quadruped orientation \mathbf{R}_Q and tail base orientation \mathbf{R}_B are defined in Eq. (1), along with the tail link orientations $\mathbf{R}_{T,i}^B$ relative to \mathbf{R}_B (vectors/matrices defined with respect to \mathbf{R}_B are labeled with a B superscript), where $\mathbf{R}_Z(\gamma)$ denotes a Z -axis rotation matrix for angle γ :

$$\begin{aligned} \mathbf{R}_Q &= \mathbf{R}_Z(\varphi), \\ \mathbf{R}_B &= \mathbf{R}_Q \mathbf{R}_Z(180 \text{ deg}), \\ \mathbf{R}_{T,i}^B &= \begin{cases} \mathbf{R}_Z(\theta_i), & i = 1 \\ \mathbf{R}_{T,i-1}^B \mathbf{R}_Z(\theta_i) & i > 1 \end{cases} \end{aligned} \quad (1)$$

The positions of the quadruped \mathbf{p}_Q and tail base \mathbf{p}_B are defined in Eq. (2), where d_{Q2B} is the distance from the quad COM to the tail base. The positions from the tail base to the tail's joint i ($\mathbf{p}_{T,i}^B$) and link i COM ($\mathbf{p}_{L,i}^B$) are defined in Eq. (3), where L_L is the distance between joints on a link. The angular velocities of the quad relative to ground (ω_Q) and tail links relative to \mathbf{R}_B ($\omega_{T,i}^B$) are defined in Eq. (4), where \dot{b} denotes the time derivative of b :

$$\mathbf{p}_Q = [x \ y \ 0]^T, \quad \mathbf{p}_B = \mathbf{p}_Q - d_{Q2B} \mathbf{R}_Q \mathbf{x} \quad (2)$$

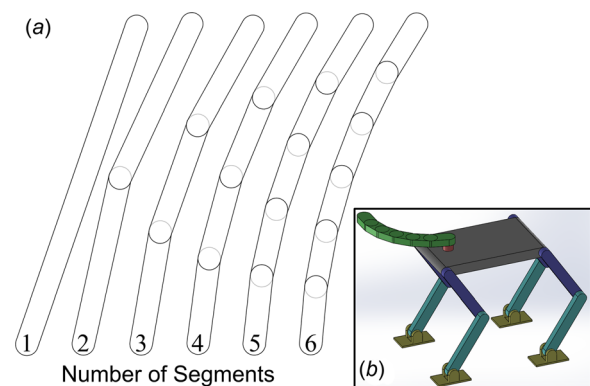


Fig. 1 (a) One-through 6DOF tail structures and (b) 6DOF tail mounted to quadruped

Contributed by the Dynamic Systems Division of ASME for publication in the JOURNAL OF DYNAMIC SYSTEMS, MEASUREMENT, AND CONTROL. Manuscript received September 22, 2015; final manuscript received March 7, 2016; published online May 25, 2016. Assoc. Editor: Jongeun Choi.

$$\mathbf{p}_{J,i}^B = \begin{cases} 0, & i = 1 \\ \mathbf{p}_{J,i}^B + L_L \mathbf{R}_{T,i-1}^B \mathbf{x}, & i > 1 \end{cases} \quad \mathbf{p}_{L,i}^B = \mathbf{p}_{J,i}^B + 0.5L_L \mathbf{R}_{T,i}^B \mathbf{x} \quad (3)$$

$$\omega_Q = \dot{\phi} \mathbf{R}_Q \mathbf{z}, \quad \omega_{T,i}^B = \begin{cases} \dot{\theta}_i \mathbf{R}_{T,i}^B \mathbf{z}, & i = 1 \\ \omega_{T,i-1}^B + \dot{\theta}_i \mathbf{R}_{T,i}^B \mathbf{z}, & i > 1 \end{cases} \quad (4)$$

Angular accelerations α_Q and $\alpha_{T,i}^B$ may be calculated by taking the first-time derivative of Eq. (4). Linear velocities $\mathbf{v}_{J,i}^B$ and $\mathbf{v}_{L,i}^B$, and linear accelerations $\mathbf{a}_{J,i}^B$ and $\mathbf{a}_{L,i}^B$ may be calculated by taking the first- and second-time-derivatives of Eq. (3).

2.2 Tail Dynamics. It is assumed that there is an actuation mechanism onboard the tail to generate the desired tail motion and the actuation's effect on the tail is entirely captured in the tail inertia. A recursive approach is used to calculate the joint forces $\mathbf{F}_{J,i}$ and moments $\mathbf{M}_{J,i}$ to formulate the base tail loading. Calculating from the link n to link 1, Eqs. (5) and (6) define $\mathbf{F}_{J,i}$ and $\mathbf{M}_{J,i}$ using the Newton–Euler equations, where $m_{L,i}$ is the link i mass, $I_{zz,L,i}$ is the link i z-axis moment of inertia, $\mathbf{p}_{L2J,i,j}^B$ is defined in Eq. (7), and the notation $\tilde{\mathbf{p}}\mathbf{F}$ denotes the cross product $\mathbf{p} \times \mathbf{F}$. The tail loading on the quad at the base (\mathbf{F}_B and \mathbf{M}_B) is defined in Eq. (8):

$$\mathbf{F}_{J,i}^B = \begin{cases} m_{L,i} \mathbf{a}_{L,i}^B, & i = n \\ \mathbf{F}_{J,i+1}^B + m_{L,i} \mathbf{a}_{L,i}^B, & i < n \end{cases} \quad (5)$$

$$\mathbf{M}_{J,i}^B = \begin{cases} I_{zz,L,i} \alpha_{T,i}^B - \tilde{\mathbf{p}}_{L2J,i,i}^B \mathbf{F}_{J,i}^B, & i = n \\ \mathbf{M}_{J,i+1}^B + I_{zz,L,i} \alpha_{T,i}^B + \tilde{\mathbf{p}}_{L2J,i,i+1}^B \mathbf{F}_{J,i+1}^B - \tilde{\mathbf{p}}_{L2J,i,i}^B \mathbf{F}_{J,i}^B, & i < n \end{cases} \quad (6)$$

$$\mathbf{p}_{L2J,i,j}^B = \mathbf{p}_{J,j}^B - \mathbf{p}_{L,i}^B \quad (7)$$

$$\mathbf{F}_B = -\mathbf{R}_B \mathbf{F}_{J,1}^B, \quad \mathbf{M}_B = -\mathbf{R}_B \mathbf{M}_{J,1}^B \quad (8)$$

2.3 Quadraped Dynamics. The quadraped's governing equations are defined in Eq. (9), where m is the system mass, I_{zz} is the system z-axis inertia, \mathbf{a}_{COM} is the system COM acceleration, \mathbf{F}_T and $M_{z,T}$ are the net tail loading, and \mathbf{F}_F and $M_{z,F}$ are the foot contact friction loading:

$$m \mathbf{a}_{\text{COM}} = \mathbf{F}_T + \mathbf{F}_F, \quad I_{zz} \ddot{\phi} = M_{z,T} + M_{z,F} \quad (9)$$

The system mass m and center-of-mass position \mathbf{p}_{COM} are calculated using Eq. (10), where m_Q is the quadraped's mass; \mathbf{a}_{COM} is calculated by differentiating \mathbf{p}_{COM} twice, I_{zz} is calculated using Eq. (11), where $I_{zz,Q}$ is the quadraped's z-axis inertia at its COM,

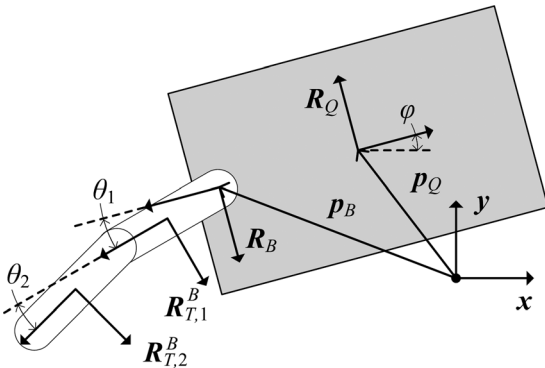


Fig. 2 Reference frames and coordinates for 2DOF tail and quad

and \mathbf{p}_{C2Q} and $\mathbf{p}_{C2L,i}$ are defined in Eq. (12). The net tail loading (\mathbf{F}_T and $M_{z,T}$) is due to the base loading \mathbf{F}_B and \mathbf{M}_B , as shown in Eq. (13):

$$m = m_Q + \sum_{i=1}^n m_{L,i}, \quad (10)$$

$$\mathbf{p}_{\text{COM}} = \left(m_Q \mathbf{p}_Q + \sum_{i=1}^n m_{L,i} (\mathbf{p}_B + \mathbf{R}_B \mathbf{p}_{L,i}^B) \right) / m$$

$$I_{zz} = I_{zz,Q} + m_Q \|\mathbf{p}_{C2Q}\|^2 + \sum_{i=1}^n (I_{zz,L,i} + m_{L,i} \|\mathbf{p}_{C2L,i}\|^2) \quad (11)$$

$$\mathbf{p}_{C2Q} = \mathbf{p}_Q - \mathbf{p}_{\text{COM}}, \quad \mathbf{p}_{C2L,i} = \mathbf{p}_B + \mathbf{R}_B \mathbf{p}_{L,i}^B - \mathbf{p}_{\text{COM}} \quad (12)$$

$$\mathbf{F}_T = \mathbf{F}_B, \quad M_{z,T} = \mathbf{z} \cdot \mathbf{M}_B + \mathbf{z} \cdot (\tilde{\mathbf{p}}_B - \tilde{\mathbf{p}}_{\text{COM}}) \mathbf{F}_B \quad (13)$$

The friction loading (\mathbf{F}_F and $M_{z,F}$) is simulated using a stiction model to represent the static and dynamic friction effects. This friction resists both linear (\mathbf{v}_Q , derivative of Eq. (2)) and rotational ($\dot{\phi}$) quadraped velocities. The maximum friction force $F_{F,\text{max}}$ and moment $M_{z,F,\text{max}}$ magnitudes are calculated in Eq. (14), where μ_s and μ_d are the static and dynamic coefficients of friction, respectively, g is gravitational acceleration, and L_F is the effective friction moment arm:

$$\mathbf{F}_{F,\text{max}} = \begin{cases} \mu_s mg, & \|\mathbf{v}_Q\| = 0 \\ \mu_d mg, & \|\mathbf{v}_Q\| \neq 0 \end{cases}, \quad M_{z,F,\text{max}} = \begin{cases} \mu_s mg L_F, & \dot{\phi} = 0 \\ \mu_d mg L_F, & \dot{\phi} \neq 0 \end{cases} \quad (14)$$

Two variables control the friction loading for translation and rotation: contact velocity and tail loading (\mathbf{v}_Q and \mathbf{F}_T for translation; $\dot{\phi}$ and $M_{z,T}$ for rotation). Equations (15) and (16) define \mathbf{F}_F and $M_{z,F}$, where $\hat{\mathbf{X}} = \mathbf{X}/\|\mathbf{X}\|$ for vectors and $\hat{x} = x/|x|$ for scalars:

$$\mathbf{F}_F = \begin{cases} -\mathbf{F}_T & \|\mathbf{v}_Q\| = 0, \|\mathbf{F}_T\| < F_{F,\text{max}} \\ -F_{F,\text{max}} \hat{\mathbf{F}}_T & \|\mathbf{v}_Q\| = 0, \|\mathbf{F}_T\| \geq F_{F,\text{max}} \\ -F_{F,\text{max}} \hat{\mathbf{v}}_Q & \|\mathbf{v}_Q\| \neq 0 \end{cases} \quad (15)$$

$$M_{z,F} = \begin{cases} -M_{z,T} & |\dot{\phi}| = 0, |M_{z,T}| < F_{F,\text{max}} \\ -M_{F,\text{max}} \hat{M}_{z,T} & |\dot{\phi}| = 0, |M_{z,T}| \geq F_{F,\text{max}} \\ -M_{F,\text{max}} \hat{\dot{\phi}} & |\dot{\phi}| \neq 0 \end{cases} \quad (16)$$

In order to calculate L_F , a model for the quadraped's contact force distribution among its feet is needed. Figure 3 illustrates a top-view schematic of the quad, showing the four points (1–4) at which the feet contact the ground. The positions $\mathbf{p}_{F,i}$ of the feet relative to the system COM are defined in Eq. (17), where \mathbf{p}_{Q2C}^Q is

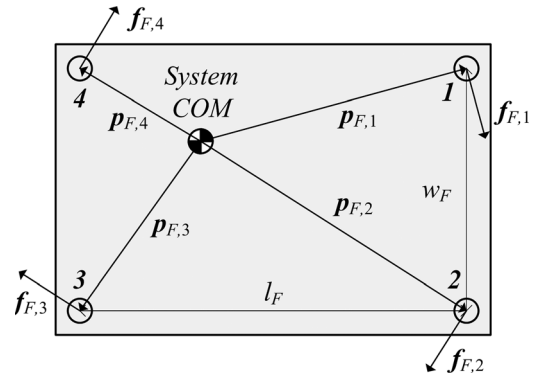


Fig. 3 Foot contact forces and friction moment effective length calculation parameters

the position of the quadruped centroid relative to the quadruped COM, and l_F and w_F are the x - and y -axis separation of the feet. The friction forces $f_{F,i}$ generated in response to $M_{z,T}$ lead to a moment relative to the system COM for which the magnitude may be represented by $\mu mg L_F$, shown in Eq. (18), which captures the geometric properties of $p_{F,i}$ and $f_{F,i}$ in L_F . This leads to Eq. (19), where $f_{C,i}$ is the fraction of system weight supported at foot i . The Appendix presents the model used to calculate $f_{C,i}$:

$$p_{F,i} = p_Q + R_Q \left(p_{Q2C}^O + x_{F,i} x + y_{F,i} y \right) - p_{COM}$$

$$x_{F,i} = \begin{cases} 0.5l_F & i = \{1, 2\} \\ -0.5l_F & i = \{3, 4\} \end{cases}, \quad y_{F,i} = \begin{cases} 0.5w_F & i = \{1, 4\} \\ -0.5w_F & i = \{2, 3\} \end{cases} \quad (17)$$

$$\sum_{i=1}^4 \|\tilde{p}_{F,i} f_{F,i}\| = \mu mg L_F \quad (18)$$

$$L_F = \sum_{i=1}^4 f_{C,i} \|p_{F,i}\| \quad (19)$$

3 Numerical Modeling and Trajectory Planning

This section describes how the mathematical model is implemented in Simulink, defines an additional multibody dynamics system model, and presents the method used to calculate the tail joint angle trajectories.

3.1 Simulink Implementation. Simulink was chosen to implement the system model because of the stiction model requirements. For the rotational stiction model, if $\dot{\varphi}$ would change sign, it is instead set to zero to trigger static friction. The Integrator block in Simulink has a “state port” option that allows precalculation of $\dot{\varphi}$ to check if it would change sign. If it would, the model sets the integrator output to zero instead.

3.2 Multibody Dynamics System Model. In addition to the Simulink model, a multibody dynamics model implemented in MSC ADAMS is also generated to compare results. The ADAMS model utilizes the computer-aided design geometry (Fig. 1(b)) and mass properties of the quad and tail models used to generate the simulation parameters (Sec. 4.1). Tail joint angle trajectories are prescribed, contact friction models are included at the four feet, and the resulting quadruped motion is calculated.

A key difference between the Simulink and ADAMS models is the friction implementation. In the Simulink model, a “pure” stiction model is implemented, for which loading must overcome static friction before motion begins. However, in the ADAMS model, a variable coefficient of friction depending on the contact velocity between the foot and ground is used, as shown in Fig. 4. Instead of a discontinuity, the friction coefficient uses continuous

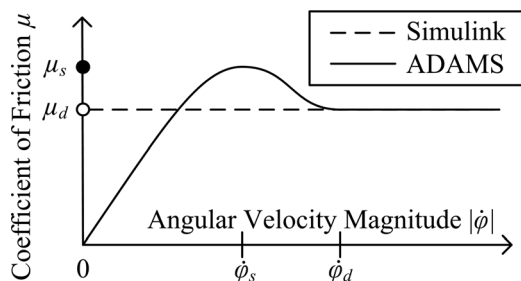


Fig. 4 Friction coefficient profiles for stiction (Simulink) and continuous (ADAMS) models

step functions: a half-step from 0 to μ_s over the range $[0, \dot{\theta}_s]$, and a full-step from μ_s to μ_d over the range $[\dot{\theta}_s, \dot{\theta}_d]$.

The quad structure design is implemented in SOLIDWORKS, and exported to ADAMS. The quadruped’s leg joints (hip, knee, and ankle) are fixed during the simulation. The tail trajectory is generated in a MATLAB script and imported to ADAMS as a spline of the tail’s angular velocity. This prescribed angular velocity profile is applied to the tail with the appropriate initial angle condition.

3.3 Trajectory Planning. With the stiction model, static friction can be considered a high-pass filter for tail loading—if F_T or $M_{z,T}$ cannot overcome static friction, the system will not translate or rotate, respectively. Therefore, if the loading direction causing undesired rotation can be minimized, tail performance can be improved.

For motion between two stationary tail positions, the integral of the joint acceleration is zero. However, by changing the relative time over which acceleration and deceleration occur, their relative magnitudes may be altered. Previous research has utilized split-cycle frequency modulation [24] to control micro air vehicles by prescribing different wing velocities for up and down flaps. This approach may be adapted for acceleration/deceleration of robotic tails.

Figure 5 illustrates an example of the joint angular acceleration profile defined in Eq. (20), with a shorter acceleration duration $\Delta_a = t_1 - t_0$ and a longer deceleration duration $\Delta_d = t_2 - t_1$. Equation (21) shows the parameterization of Δ_a and Δ_d by the total period ΔT and split-cycle parameter w_{ss} ranging from 0 to 1

$$\ddot{\theta} = \begin{cases} A \sin(\pi(t - t_0)/\Delta_a), & t_0 \leq t \leq t_1 \\ -B \sin(\pi(t - t_1)/\Delta_d), & t_1 < t \leq t_2 \end{cases} \quad (20)$$

$$\Delta T = t_2 - t_0, \quad \Delta_a = w_{ss} \Delta T, \quad \Delta_d = \Delta T - \Delta_a \quad (21)$$

Boundary conditions for the tail trajectory are defined in Eq. (22), where θ_0 is the initial angle and $\Delta\theta$ is the tail’s angular displacement. Integrating Eq. (20) using Eq. (22), expressions for A and B are found, shown in the following equation:

$$\theta(t_0) = \theta_0, \quad \theta(t_2) = \theta_0 + \Delta\theta, \quad \dot{\theta}(t_0) = \dot{\theta}(t_2) = 0 \quad (22)$$

$$A \Delta_a = B \Delta_d, \quad A = \frac{\pi \Delta\theta}{w_{ss} (\Delta T)^2}, \quad B = \frac{\pi \Delta\theta}{(1 - w_{ss}) (\Delta T)^2} \quad (23)$$

4 Case Studies

This section defines the simulation parameters, compares the mathematical and multibody dynamics models, and utilizes the mathematical model to study the impact of tail structure and trajectory on the net quadruped rotation φ_{net} .

4.1 Simulation Parameters. The quadruped simulation parameters (Table 1) are determined based on the generic quadruped structure shown in Fig. 1(b), with parts defined as aluminum,

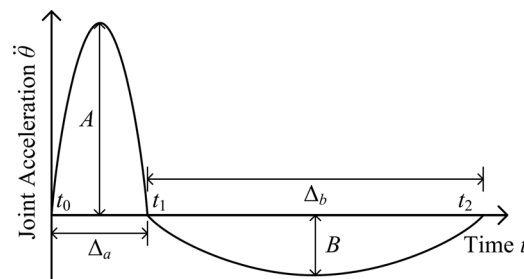


Fig. 5 Split-cycle acceleration profile

Table 1 Quadraped properties

m_Q	8.458 kg	$I_{zz,Q}$	0.1916 kg/m ²	μ_d	0.30
d_{Q2B}	0.125 m	d_{Q2C}	-0.0155 m	μ_s	0.25
l_F	0.3 m	w_F	0.26 m		
$\dot{\varphi}_s$	0.05 rad/s	$\dot{\varphi}_d$	0.5 rad/s		

Table 2 Tail properties

n	m_L (kg)	$I_{zz,L}$ (kg/m ²)	L_L (m)
1	2.40	2.236×10^{-2}	0.300
2	1.20	3.469×10^{-3}	0.150
3	0.80	1.268×10^{-3}	0.100
4	0.60	6.521×10^{-4}	0.075
5	0.48	4.022×10^{-4}	0.060
6	0.40	2.743×10^{-4}	0.050

and estimates for the friction parameters. The tail simulation parameters (Table 2) are defined such that each tail is 300 mm long and 2.4 kg in mass, with link quantity varying from one to six.

4.2 Model Comparison. The Simulink and ADAMS models are compared to quantify their difference in simulating the quadraped system with tail. Two cases are considered: a 1DOF tail and a 6DOF tail. Each simulation's tail joint trajectory is defined by $\Delta T = 0.25$, $\theta_0 = 0$ deg and $w_{ss} = 0.25$ with $\Delta\theta = -90$ deg and

$\Delta\theta = -30$ deg for the 1DOF and 6DOF simulations, respectively, with $d_{Q2B} = 140.5$.

Results are shown in Fig. 6. In both cases, the Simulink model rotates less than the ADAMS model, due to the friction modeling. In the ADAMS model, when $\dot{\varphi} = 0$, $\mu(\dot{\varphi}) = 0$, leading to zero friction. This reduces the resistance to rotation in that model, resulting in greater predicted rotation. As a result, the Simulink model is a more conservative estimate for system rotation and will be used in Secs. 4.3–4.7.

4.3 Loading Analysis. For a trajectory defined by $\Delta T = 0.25$, $\Delta\theta = -90$ deg, $\theta_0 = 0$ deg, and $w_{ss} = 0.25$ using the 1DOF tail model, the resulting quadraped rotation trajectory $\varphi(t)$ is shown in Fig. 7(a). The associated $M_{z,T}$, $M_{z,F}$, and $I_{zz}\ddot{\varphi}$ are shown in Fig. 7(b) and key phases of these trajectories are denoted A–D.

During A, $M_{z,T}$ is positive, leading to positive $\ddot{\varphi}$ after overcoming static friction with constant dynamic friction resistance. However, $M_{z,T}$ dips below zero at the end of the phase due to the tail's centripetal force when $\dot{\theta}$ is near zero. In B, $M_{z,T}$ is negative, but $\dot{\varphi}$ is positive. $M_{z,T}$ and $M_{z,F}$ both act in opposition to the positive $\dot{\varphi}$, until it reaches zero at the end of B. At the beginning of C, $\dot{\varphi}$ becomes negative when $M_{z,T}$ overcomes static $M_{z,F}$. During D, $M_{z,T}$ is zero, but $M_{z,F}$ opposes the negative $\dot{\varphi}$ until $\dot{\varphi} = 0$.

4.4 Actuation Effectiveness. The tail's effectiveness in transmitting loading to the quad is controlled by two parameters for a given tail and quad: d_{Q2B} and θ . For the 1DOF tail, Eq. (24) expands Eq. (13) to show $M_{z,T}$ explicitly in terms of d_{Q2B} and θ :

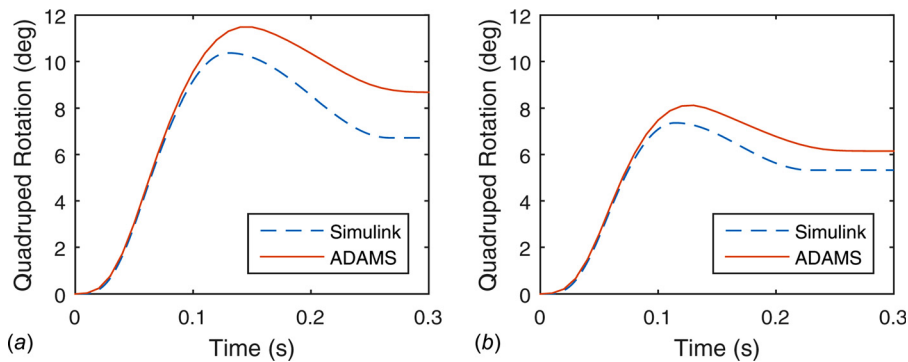


Fig. 6 Comparison of Simulink and ADAMS model φ trajectories for (a) 1DOF tail and (b) 6DOF tail

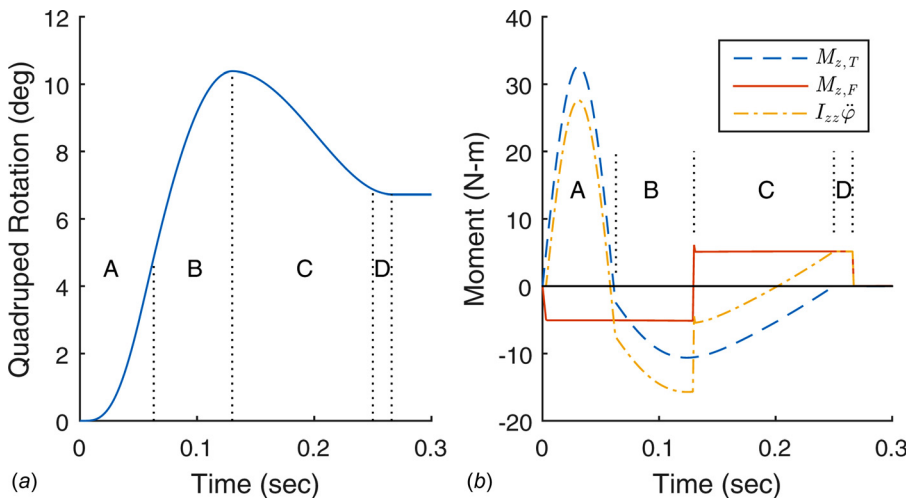


Fig. 7 (a) φ trajectory and (b) associated tail, friction, and inertial moments for 1DOF tail

$$M_{z,T} = -\left(I_{zz,L} + 0.25m_L L_L^2 \frac{m_Q}{m}\right)\ddot{\theta} + M_{z,T,\tan} + M_{z,T,\text{cen}}$$

$$M_{z,T,\tan} = -I_{\text{eff}}\ddot{\theta}c_{\theta} \quad M_{z,T,\text{cen}} = I_{\text{eff}}\dot{\theta}^2 s_{\theta} \quad I_{\text{eff}} = \frac{m_Q m_L}{2m} L_L d_{Q2B}$$
(24)

$M_{z,T}$ consists of three terms: (1) the rotational moment (d_{Q2B} - and θ -invariant), (2) the moment $M_{z,T,\tan}$ due to the tail's tangential acceleration force, and (3) the moment $M_{z,T,\text{cen}}$ due to the tail's centripetal force. $M_{z,T,\tan}$ and $M_{z,T,\text{cen}}$ are linearly dependent on d_{Q2B} , implying that d_{Q2B} should be maximized. In terms of joint angle, within the range $\theta \in [-90 \text{ deg}, 90 \text{ deg}]$, $|M_{z,T,\tan}|$ is maximized at $\theta = 0$, but $|M_{z,T,\text{cen}}|$ is maximized at $\theta = \pm 90 \text{ deg}$. The $\dot{\varphi}$ contribution of these moments (i.e., $M_{z,T,\tan}/I_{zz}$ and $M_{z,T,\text{cen}}/I_{zz}$) is shown in Fig. 8 for $d_{Q2B} = 0.125 \text{ m}$, $\dot{\theta} = 1 \text{ rad/s}$, and $\ddot{\theta} = 1 \text{ rad/s}^2$. Therefore, joint acceleration matching the desired φ_{net} direction should bias toward $\theta = 0 \text{ deg}$, and maximum joint velocities should bias toward $\theta = \pm 90 \text{ deg}$ depending on the desired moment direction.

Given this transmission dependence on θ during motion, for a prescribed tail acceleration profile, the initial angle θ_0 plays a significant role. A tail trajectory defined by $\Delta T = 0.25$, $\Delta\theta = -90 \text{ deg}$, and $w_{ss} = 0.25$ with $\theta_0 \in [0 \text{ deg}, 90 \text{ deg}]$ and $d_{Q2B} \in [0, 0.15] \text{ m}$ is prescribed. By varying θ_0 , the joint velocity/acceleration profiles remain constant but are applied over different ranges of θ . Figure 9 shows the resulting φ_{net} rotations for these simulation parameters, where θ_0 and d_{Q2B} are specified in 15 deg and 0.025 m increments.

As predicted, increasing d_{Q2B} consistently increases φ_{net} due to the increased length over which the tail forces are amplified. In terms of initial angle, the trade-off between maximizing tangential effects (lower θ_0) and centripetal effects (higher θ_0) biases slightly in favor of centripetal effects, as evidenced by the maximum φ_{net} primarily occurring when $\theta_0 = 60 \text{ deg}$.

In addition, L_F also changes as a function of d_{Q2B} and θ , as shown in Fig. 10. However, maximum variation from the range's median is less than 3%, so changes in L_F have minimal impact.

4.5 Split-Cycle Parameter Modification. A tail trajectory defined by $\Delta T = 0.25 \text{ s}$, $\Delta\theta = -90 \text{ deg}$, and $\theta_0 = 45 \text{ deg}$ with $w_{ss} \in [0.1, 0.9]$ is used to analyze the impact of the split-cycle parameter. Figure 11 shows φ_{net} when w_{ss} is varied in 0.1 increments from 0.1 to 0.9. As expected, lower w_{ss} correlates to a higher net rotation. This is due to (1) the increased disparity between angular acceleration magnitudes in the desired/undesired directions (discussed in Sec. 3.3) and (2) the angular velocity bias in the $\theta > 0$ range. Maximum velocity occurs at $t = w_{\text{mod}}\Delta T$ and $\theta(w_{\text{mod}}\Delta T) = \theta_0 + w_{\text{mod}}\Delta\theta$. Therefore, by lowering w_{ss} , the θ associated with the maximum velocity increases, increasing the desired moment due to centripetal forces according to Eq. (24).

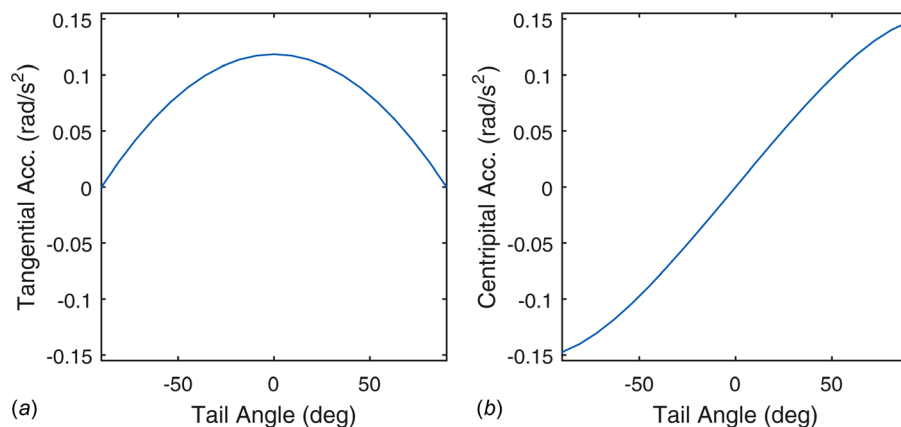


Fig. 8 Comparison of (a) tangential and (b) centripetal contributions to $\dot{\varphi}$

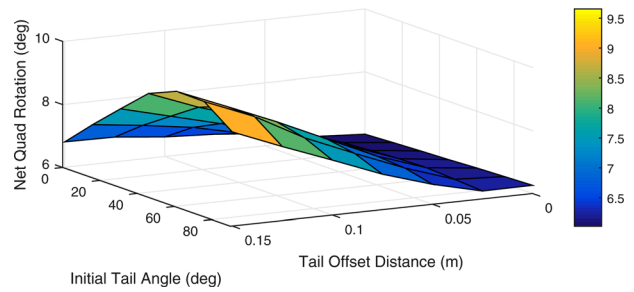


Fig. 9 Net φ rotation for varying θ_0 and d_{Q2B}

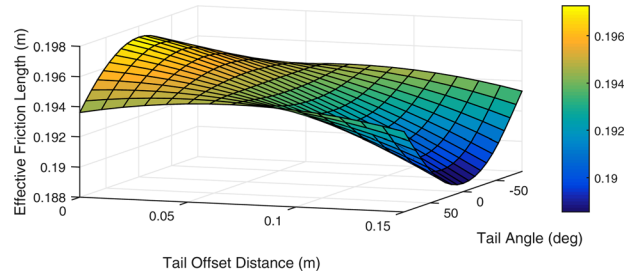


Fig. 10 L_F for varying θ and d_{Q2B}

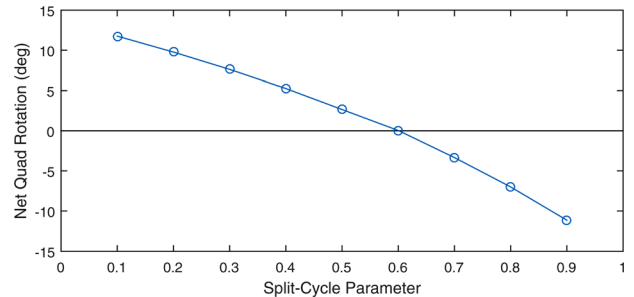


Fig. 11 Net φ rotation for varying w_{ss}

4.6 Maximum Tail Velocity. Two factors influence a tail's maximum angular velocity for a fixed w_{ss} : $\Delta\theta$ and ΔT . A tail trajectory defined by $w_{ss} = 0.25$ and $\theta_0 = 90 \text{ deg}$ with $\Delta T \in [0.1, 0.6]$ and $\Delta\theta \in [60 \text{ deg}, 180 \text{ deg}]$ is used to analyze the impact of maximum tail velocity. Figure 12 illustrates the net φ rotation when ΔT and $\Delta\theta$ are varied at 0.05 s and 30 deg increments. As expected, as $\Delta\theta$ increases and/or ΔT decreases, φ_{net} increases.

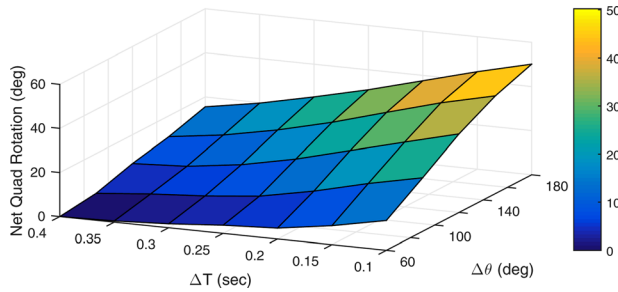


Fig. 12 Net φ rotation for varying ΔT and $\Delta\theta$

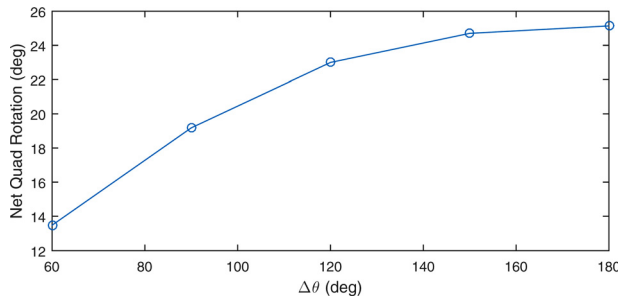


Fig. 13 Comparison of net φ rotation for constant maximum tail velocity

The impact of the centripetal acceleration is observed when considering the tradeoff between $\Delta\theta$ and ΔT , if the tail's maximum velocity ($2\Delta\theta/\Delta T$) is held constant. Figure 13 illustrates φ_{net} for different values of $\Delta\theta$, with a correlated ΔT that results in 10.47 rad/s (600 deg/s) maximum velocity. The relative benefit of the higher $\Delta\theta$ primarily stems from the increased ΔT over which the centripetal forces act during the tail motion.

4.7 Tail DOF. This section compares the performance of different tail configurations, ranging from 1DOF to 6DOF. A key challenge in comparing tails with different DOFs is choosing joint trajectories for each tail that allow a fair comparison.

To accomplish this, two constraints will be set on the tail trajectory: (1) the tail will move between the two extreme configurations for the given number of tail segments and (2) joint angle trajectories will have the same maximum joint velocity. Equation (25) defines the $\Delta\theta$ associated moving the n -link tail tip clockwise from the negative y -axis to the positive y -axis, and the ΔT necessary to prescribe the maximum joint velocity $|\dot{\theta}_{\text{max}}|$ (10.47 rad/s for these simulations):

$$\Delta\theta = -360 \text{ deg}/(n+1) \quad \Delta T = 2\Delta\theta/|\dot{\theta}_{\text{max}}| \quad (25)$$

Figure 14 shows φ_{net} for an n -segment tail with trajectories defined by ΔT and $\Delta\theta$ from Eq. (25), $\theta_0 = 0.5\Delta\theta$, and $w_{ss} = 0.25$. The increase in φ_{net} with n is due to: (1) the compounded angular

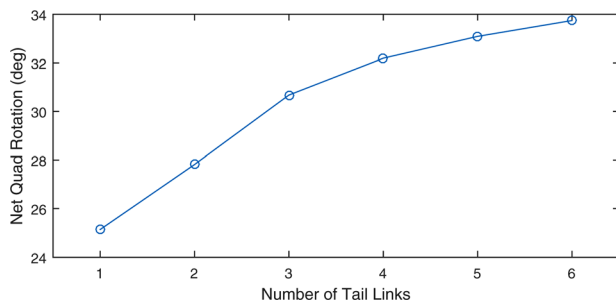


Fig. 14 Net φ rotation for tails with varying DOF

acceleration toward the tip disk and (2) the axial motion of the tail segments when $n > 1$. After differentiating Eq. (4), it is obvious that each link's angular acceleration includes the acceleration of its preceding links. The axial motion is due to the change in radial distance between each link's COM during the trajectory. For example, for the 6DOF tail, when $\theta = 30$ deg, the link 6 COM is 209.4 mm from the base frame, whereas when $\theta = 0$ deg, the COM is 275 mm from the base frame.

5 Conclusion

This paper has analyzed the effect a planar robotic tail's design and trajectory factors have on a quadruped's yaw-angle steering. A key goal of this paper has been to better understand, both qualitatively and quantitatively, how the design and use of tail-like structures onboard mobile robot impacts its maneuverability. Significant results of the analysis include the demonstration of the relatively equal importance of the tail's centripetal and tangential inertial force loading for trajectory planning (with centripetal loading slightly more important), the benefit of split-cycle frequency modulation for controlling the relative magnitude of joint acceleration, and the benefit of multi-DOF tail structures. This work will aid both designing future tail-assisted mobile robots (e.g., optimizing tail mounting location) and operating them (i.e., for a given design, finding the optimal trajectory for generating a desired yaw rotation).

5.1 Future Work. Future work will focus on full-scale implementation and analysis of tail-like structures onboard mobile robots. Various serpentine robotic structures that are capable of spatial motion will be considered. Both "rigid-structure" (links kinematically coupled by gears or cabling) and "elastic-structure" (links mechanically coupled by springs) serpentine tails are under consideration. Actuation for these serpentine tails will be cabling routed along the length controlled by motors at the actuation base. Control algorithms will be developed to enable the tail to perform a variety of functions onboard the system, including both maneuvering (e.g., turning) and stabilizing (e.g., rejecting disturbance loading and preventing tipping), with an emphasis on performing these tasks during locomotion. Different sensing strategies will be considered to measure the real-time performance of the tail and enable feedback during use.

Acknowledgment

This material is based upon work supported by the National Science Foundation under Grant No. 1557312.

Appendix: Foot Contact Forces

For a given \mathbf{p}_{COM} , the model must calculate the contact force distribution $f_{C,i}$ for the quadruped's four feet. This distribution should change continuously with \mathbf{p}_{COM} , not result in negative contact forces, and satisfy the quadruped equilibrium conditions in the following equation:

$$\begin{aligned} \sum_{i=1}^4 f_{C,i} &= 1 \\ (0.5l_F - x)(f_{C,1} + f_{C,2}) &= (0.5l_F + x)(f_{C,3} + f_{C,4}) \\ (0.5w_F - y)(f_{C,1} + f_{C,4}) &= (0.5w_F + y)(f_{C,2} + f_{C,3}) \end{aligned} \quad (A1)$$

To accomplish this, for a given \mathbf{p}_{COM} , a position vector \mathbf{p}_{C2C}^Q is found from the quad centroid to the system COM relative to \mathbf{R}_Q , defined in Eq. (A2), where \mathbf{R}_Q^T is the transpose of \mathbf{R}_Q and d_{Q2C} is the x -axis displacement from the quad COM to the quad centroid. Using \mathbf{p}_{C2C}^Q , ellipse parameters a , b , and ζ may be found using Eq. (A3) ($a, b \geq 0$)

$$\mathbf{p}_{C2C}^0 = \mathbf{R}'_Q(\mathbf{p}_{COM} - \mathbf{p}_Q - d_{Q2C}\mathbf{x}) \quad (\text{A2})$$

$$x_e = \mathbf{p}_{C2C}^0 \cdot \mathbf{x}, \quad y_e = \mathbf{p}_{C2C}^0 \cdot \mathbf{y} \quad (\text{A3})$$

$$x_e = a \cos \xi, \quad y_e = b \sin \xi, \quad a/b = l_F/w_F$$

Equation (A4) presents an empirically derived contact force formulation, with the associated coefficients in Eq. (A5). These coefficients were calculated by analyzing the static equilibrium at $\xi = [0, 90, 180, 270]$ and fitting Eq. (A4) to match those points:

$$f_{c,i}(\xi) = A + B \sin(\xi + C_i) \quad (\text{A4})$$

$$A = \frac{1}{4}, \quad B = \frac{b\sqrt{2}}{2w_F}, \quad C_1 = 45 \text{ deg}, \quad C_2 = 135 \text{ deg}, \quad C_3 = 225 \text{ deg}, \quad C_4 = 315 \text{ deg} \quad (\text{A5})$$

This model meets the three requirements (continuous distribution, non-negative contact forces, and static equilibrium) if $b \leq 0.5w_F$. However, if $b > 0.5w_F$, at least one of the contact force will be negative. If this is the case, the negative contact force(s) should be set to zero, and the remaining contact forces can be solved directly from the static equilibrium conditions defined in Eq. (A1).

References

- [1] Wilson, A. M., Lowe, J. C., Roskilly, K., Hudson, P. E., Golabek, K. A., and McNutt, J. W., 2013, "Locomotion Dynamics of Hunting in Wild Cheetahs," *Nature*, **498**(7453), pp. 185–189.
- [2] Jusufi, A., Kawano, D. T., Libby, T., and Full, R. J., 2010, "Righting and Turning in Mid-Air Using Appendage Inertia: Reptile Tails, Analytical Models and Bio-Inspired Robots," *Bioinspiration Biomimetics*, **5**(4), p. 045001.
- [3] Fish, F. E., Bostic, S. A., Nicastro, A. J., and Beneski, J. T., 2007, "Death Roll of the Alligator: Mechanics of Twist Feeding in Water," *J. Exp. Biol.*, **210**(16), pp. 2811–2818.
- [4] Walker, C., Vierck, C. J., Jr., and Ritz, L. A., 1998, "Balance in the Cat: Role of the Tail and Effects of Sacrocaudal Transaction," *Behav. Brain Res.*, **91**(1–2), pp. 41–47.
- [5] O'Connor, S. M., Dawson, T. J., Kram, R., and Donelan, J. M., 2014, "The Kangaroo's Tail Propels and Powers Pentapedal Locomotion," *Biol. Lett.*, **10**(7), p. 20140381.
- [6] Bezanson, M., 2012, "The Ontogeny of Prehensile-Tail Use in *Cebus capucinus* and *Alouatta palliata*," *Am. J. Primatol.*, **74**(8), pp. 770–782.
- [7] Johnson, A. M., Libby, T., Chang-Siu, E., Tomizuka, M., Full, R. J., and Koditschek, D. E., 2012, "Tail Assisted Dynamic Self Righting," *Conference on Climbing and Walking Robots and Support Technologies for Mobile Machines*, Baltimore, MD, pp. 611–620.
- [8] Chang-Siu, E., Libby, T., Tomizuka, M., and Full, R. J., 2011, "A Lizard-Inspired Active Tail Enables Rapid Maneuvers and Dynamic Stabilization in a Terrestrial Robot," *IEEE/RSJ International Conference on Intelligent Robots and Systems*, San Francisco, CA, Sept. 25–30, pp. 1887–1894.
- [9] Zhao, J., Zhao, T., Xi, N., Cintron, F. J., Mutka, M. W., and Xiao, L., 2013, "Controlling Aerial Maneuvering of a Miniature Jumping Robot Using Its Tail," *IEEE/RSJ International Conference on Intelligent Robots and Systems*, Tokyo, Japan, Nov. 3–7, pp. 3802–3807.
- [10] Liu, G.-H., Lin, H.-Y., Lin, H.-Y., Chen, S.-T., and Lin, P.-C., 2014, "A Bio-Inspired Hopping Kangaroo Robot With an Active Tail," *J. Bionics Eng.*, **11**(4), pp. 541–555.
- [11] He, G., and Geng, Z., 2009, "Exponentially Stabilizing an One-Legged Hopping Robot With Non-SLIP Model in Flight Phase," *Mechatronics*, **19**(3), pp. 364–374.
- [12] Berenguer, F. J., and Monasterio-Huelin, F. M., 2008, "Zappa, a Quasi-Passive Biped Walking Robot With a Tail: Modeling, Behavior, and Kinematic Estimation Using Accelerometers," *IEEE Trans. Ind. Electron.*, **55**(9), pp. 3281–3289.
- [13] Provancher, W. R., Jensen-Segal, S. I., and Fehlberg, M. A., 2011, "ROCR: An Energy-Efficient Dynamic Wall-Climbing Robot," *IEEE/ASME Trans. Mechatron.*, **16**(5), pp. 897–906.
- [14] Patel, A., and Braae, M., 2013, "Rapid Turning at High-Speed: Inspirations From the Cheetah's Tail," *IEEE/RSJ International Conference on Intelligent Robots and Systems*, Tokyo, Japan, Nov. 3–7, pp. 5506–5511.
- [15] Casarez, C., Penskiy, I., and Bergbreiter, S., 2013, "Using an Inertial Tail for Rapid Turns on a Miniature Legged Robot," *IEEE International Conference on Robotics and Automation*, Karlsruhe, Germany, May 6–10, pp. 5469–5474.
- [16] Patel, A., and Braae, M., 2014, "Rapid Acceleration and Braking: Inspiration From the Cheetah's Tail," *IEEE International Conference on Robotics and Automation*, Hong Kong, China, May 31–June 7, pp. 793–799.
- [17] Park, H. S., Floyd, S., and Sitti, M., 2009, "Roll and Pitch Motion Analysis of a Biologically Inspired Quadruped Water Runner Robot," *Int. J. Rob. Res.*, **29**(10), pp. 1281–1297.
- [18] Briggs, R., Lee, J., Haberland, M., and Kim, S., 2012, "Tails in Biomimetic Design: Analysis, Simulation, and Experiment," *IEEE/RSJ International Conference on Intelligent Robots and Systems*, Vilamoura, Algarve, Portugal, Oct. 7–12, pp. 1473–1480.
- [19] Mutka, A., Orsag, M., and Kovacic, Z., 2013, "Stabilizing a Quadruped Robot Locomotion Using a Two Degree of Freedom Tail," *21st Mediterranean Conference on Control and Automation*, Platanias-Chania, Greece, June 25–28, pp. 1336–1342.
- [20] Rone, W. S., and Ben-Tzvi, P., 2016, "Serpentine Tail Control for Maneuvering and Stabilization of a Quadrupedal Robot," *ASME International Design Engineering Technical Conference & Computers and Information in Engineering Conference*, Charlotte, NC (under review).
- [21] Rone, W. S., and Ben-Tzvi, P., 2015, "Static Modeling of a Multi-Segment Serpentine Robotic Tail," *ASME Paper No. DETC2015-46655*.
- [22] Rone, W. S., and Ben-Tzvi, P., 2014, "Continuum Robot Dynamics Utilizing the Principle of Virtual Power," *IEEE Trans. Robot.*, **30**(1), pp. 275–287.
- [23] Rone, W. S., and Ben-Tzvi, P., 2014, "Mechanics Modeling of Multisegment Rod-Driven Continuum Robots," *ASME J. Mech. Rob.*, **6**(4), p. 041006.
- [24] Doman, D. B., Oppenheimer, M. W., and Sighthorsson, D. O., 2010, "Wingbeat Shape Modulation for Flapping-Wing Micro-Air-Vehicle Control During Hover," *J. Guid. Control Dyn.*, **33**(3), pp. 724–739.